






## Article

# Modal Parameters Estimation of Circular Plates Manufactured by FDM Technique Using Vibrometry: A Comparative Study

Martin Hagara <sup>1,\*</sup>, Miroslav Pástor <sup>1</sup>, Pavol Lengvarský <sup>1</sup>, Peter Palička <sup>1</sup> and Róbert Huňady <sup>2</sup>

<sup>1</sup> Department of Applied Mechanics and Mechanical Engineering, Faculty of Mechanical Engineering, Technical University of Košice, Letná 1/9, 042 00 Košice, Slovakia; miroslav.pastor@tuke.sk (M.P.); pavol.lengvarsky@tuke.sk (P.L.); peter.palicka@tuke.sk (P.P.)

<sup>2</sup> Department of Robotics, Faculty of Mechanical Engineering, VŠB—Technical University Ostrava, 17. Listopadu 2172/15, 708 00 Ostrava, Czech Republic; robert.hunady@vsb.cz

\* Correspondence: martin.hagara@tuke.sk

**Abstract:** This paper presents a comparative study focused on a modal parameters estimation of specimens manufactured by the FDM technique using a fixed embedded vibrometer based on the laser Doppler principle and roving hammer-impact method. Part of this paper is devoted to testing a fixed circular plate with a honeycomb infill pattern while varying the number of excitation points (DOFs), the number of analysis lines of fast Fourier transformation (FFT), and the locations or numbers of reference degrees of freedom (REFs). Although these parameters did not significantly affect the values found for the natural frequencies of the structure, there were changes in the estimates of the mode shapes (affected by the low number of DOFs), in the height and sharpness of the peaks of the CMIF functions (caused by the increased number of FFT lines), and in the number of identified modes (influenced by the chosen location(s) of REFs), respectively. Subsequently, the authors compared the results of experimental modal analyses carried out under the same conditions on three circular plates with honeycomb, star, and concentric infill patterns made of PLA. The results confirm that specimens with honeycomb or star infill patterns have a higher stiffness than those with concentric infill patterns. The low values of the damping ratios obtained for each structure indicate a strong response to excitation at or near their natural frequencies.



**Citation:** Hagara, M.; Pástor, M.; Lengvarský, P.; Palička, P.; Huňady, R. Modal Parameters Estimation of Circular Plates Manufactured by FDM Technique Using Vibrometry: A Comparative Study. *Appl. Sci.* **2024**, *14*, 10609. <https://doi.org/10.3390/app142210609>

Academic Editor: Giuseppe Lacidogna

Received: 26 October 2024  
Revised: 12 November 2024  
Accepted: 13 November 2024  
Published: 18 November 2024



**Copyright:** © 2024 by the authors. Licensee MDPI, Basel, Switzerland. This article is an open access article distributed under the terms and conditions of the Creative Commons Attribution (CC BY) license (<https://creativecommons.org/licenses/by/4.0/>).

**Keywords:** experimental modal analysis; modal parameters; laser doppler vibrometry; FDM; PLA; infill pattern; circular plate

## 1. Introduction

With the rapid development that has been achieved in the field of additive manufacturing (AM) in recent years, there is an increasing demand for the preparation and production of lightweight structures with sufficient strength and stiffness to replace various mechanical structures, e.g., structures used in the aerospace industry. In this context, the Boeing 777X, the largest twin-engine aircraft, with hundreds of 3D printed parts, which Boeing started flight-testing in 2020 [1], can be mentioned. In 2021, Pradeep et al. [2] designed a fuel injection component manufactured out of Inconel-718 nickel-based super alloy for high-temperature application in an advanced rocket propulsion system. Research results regarding missile applications, where the 3D printed coupler on the AUR missile and the parts for its fuel injector were tested, were introduced by Apalboym and Kurijaka [3], and Ramesh Kumar et al. [4], respectively. According to [5], NASA's Perseverance rover, which landed on Mars in 2021, carries 11 parts prepared with AM. The suitability of AM for the preliminary testing of surface heat exchangers used in turbofan aero-engines was confirmed in [6]. The authors suppose that AM can contribute to cost-effective, rapid, and non-intrusive testing, allowing the speeding up of the optimization process of heat exchangers. Moreover, there are some other fields, e.g., biomechanics [7–9], sensors [10–12],

the automotive industry [13–16], robotics [17–19], and even musical instruments manufacturing [20], where AM can find potential applications.

Nevertheless, despite the rapid implementation of AM, 3D printed parts, especially those that were manufactured by the fused deposition modelling (FDM) method, still have negatives such as anisotropic mechanical properties or residual stresses occurring in the printed structures due to layering of the material during the 3D printing process. The mechanical properties of various acrylonitrile butadiene styrene (ABS) and polylactic acid (PLA) components with the potential to be used for engineering applications were tested by Tymrak et al. [21]. In their study, they quantified the tensile strengths and elastic moduli of components printed using open-source 3D printers. The lack of information on the mechanical properties of parts printed using low-cost, open-source 3D printers led Lanzotti et al. [22] to quantify the ultimate tensile strength and the nominal strain at break of specimens made of PLA material with various layer thicknesses, infill orientations, and numbers of shell perimeters. Several studies have been carried out focusing on the influence of the printing orientation and layer height [23–25], fill density [25,26], printing speed [23,27], bed and nozzle temperature [28,29], raster angle [30,31], and infill pattern [25,26,32] on the quality of the FDM process. The analysis of the printing orientation, layer height, and feed rate realized in [24] showed that flat- and on-edge-oriented specimens have higher mechanical strength compared to those oriented upright. To obtain ductile behaviour of the PLA material with the optimal print time, specimen strength, and stiffness, it is recommended to correctly select a low/high layer thickness and feed rate related to the specimen orientation during printing. According to Rodríguez-Panes et al. [25], who analysed the influence of the layer height and orientation, as well as that of the fill density, the last is the parameter that influences the tensile yield stress, tensile strength, nominal strain at break, and Young's modulus of PLA and ABS specimens the most. The work provided by Hill and Haghi [30] demonstrated that the material properties such as the yield strength, tensile strength, percent elongation, Young's modulus, hardness, and density of the material are highly dependent on the raster angle. The tensile strength's dependence on the printing orientation of ABS specimens was proved also by Foltut et al. [33]. Moreover, they realized standard quasi-static tensile tests on ABS under room (23 °C) and the maximum operating (80 °C) temperature. With increasing temperature, the behaviour of the ABS changed from brittle to ductile. When comparing the 3D printed and injection-moulded specimens, the second had a 24% higher value of tensile strength. The effect of post-heat treatment on the mechanical properties of the specimen made of PLA with a 100% fill density is described in [34]. The authors concluded that this process considerably affects the fracture limit of the structure, while the effect on the tensile strength is minimal. Moreover, the Young's modulus obtained for the heat treatment above the glass transition is much higher than those obtained below the glass transition. Ale Ali et al. [35] investigated the effect of freeze–thaw cycles on the tensile, bending, and fracture resistance of specimens made of PLA material. They found that the infill ratio of PLA together with the number of freeze–thaw cycles reduced the tensile strength, flexural strength, and fracture resistance.

However, all the structures related to the above-mentioned fields are subjected to frequent vibrations or dynamic loading and it is therefore important to know their dynamic behaviour. To date, the modal and vibration response testing of AM structures has been rarely carried out. In 2017, Ozcanli [36] studied the natural frequencies of structures prepared by the FDM method. He analysed the results obtained from one experimental analysis, whereby the excitation was ensured by a modal shaker and the response was measured in one location using an accelerometer. Natural frequency values comparable to those from the numerical analysis were obtained for only a few modes. An experimental modal analysis (EMA) of several PLA beams with free-free boundary conditions was provided by Iyibilgin et al. [37]. According to their conclusions, significant changes in natural frequencies and damping ratios were obtained, relating to the variations in the fill density and infill pattern. The use of EMA as an alternative non-destructive approach for testing the mechanical properties of 3D printed beams with different infill patterns

and orientations was provided by Rajkumar [38]. The effect of the adhesion type, printing direction, and layer thickness on the vibration response and parameters obtained from EMA was analysed in [39]. The results obtained from the analysis of eight groups of ABS cantilevers showed that the adhesion type has the most significant impact. Moreover, according to the authors, neither the layer thickness nor the printing direction has a major impact on the measured dynamic modulus, natural frequencies, or damping coefficients.

The study presented in this paper describes the process of the estimation of the modal parameters of 3D printed circular plates. Unlike most of the previously published works in the field of 3D printing, the authors do not focus on comparing the results obtained under different 3D printing conditions (as mentioned in the literature review above), but instead pay attention to the aspects that can affect the accuracy of the modal parameters, i.e., mode shapes, natural frequencies, and damping ratios. For this reason, comparative measurements have been carried out using equipment specialized for modal testing, the main purpose of which was to obtain information on the optimum choice of the number of excitation points, the number and position of the response measurement locations, and the frequency resolution of the measurement. The obtained information was then used to carry out experimental modal analysis and to compare the modal parameters of PLA specimens produced with three different infill patterns (honeycomb, stars, and concentric). Since only correctly obtained and interpreted results can be further used to describe the dynamic behaviour of specimens manufactured by the FDM method, the described methodology can be further applied for more extensive research on 3D printed specimens to find a relation between the behaviour of the specimens and the conditions of their manufacture.

## 2. Materials and Methods

A white-colour PLA filament, model Creality Ender Filament PLA (Shenzhen Creality 3D Technology Co., Ltd., Shenzhen, China), with a 1.75 mm diameter was used to print the specimens. It was done using a Creality CR-10 Smart Pro (Shenzhen Creality 3D Technology Co, Shenzhen, China) 3D FDM printer with a built volume of (X) × (Y) × (Z): 300 × 300 × 400 mm<sup>3</sup>. The FDM parameters used in the manufacturing of specimens are given in Table 1.

**Table 1.** Parameters set for the manufacturing of specimens by Creality CR-10 Smart Pro printer.

Parameter	Value
Nozzle diameter	0.4 mm
Layer height	0.2 mm
Fill density	15%
Nozzle temperature	205 °C
Bed temperature	50 °C
Build orientation	flat
Top/bottom solid layers	4/4
Perimeters	3
Printing speed	60 mm/s

These parameters were set in the same manner to produce three circular specimens with different infill patterns, i.e., honeycomb (Figure 1a), stars (Figure 1b), and concentric (Figure 1c). At first, the model of a solid circular plate of thickness  $t = 3$  mm and dimensions according to Figure 1 (in mm) was generated in Solidworks 2019 (Dassault Systèmes, Paris, France). After transforming its PRT file into an STL file, the G-codes of the sliced models, containing the information about the printing parameters, infill pattern geometry, and dimensions (shown in the bottom left corners of Figure 1a–c), were generated in PrusaSlicer V2.6.1 (Prusa Research, Prague, Czech Republic).

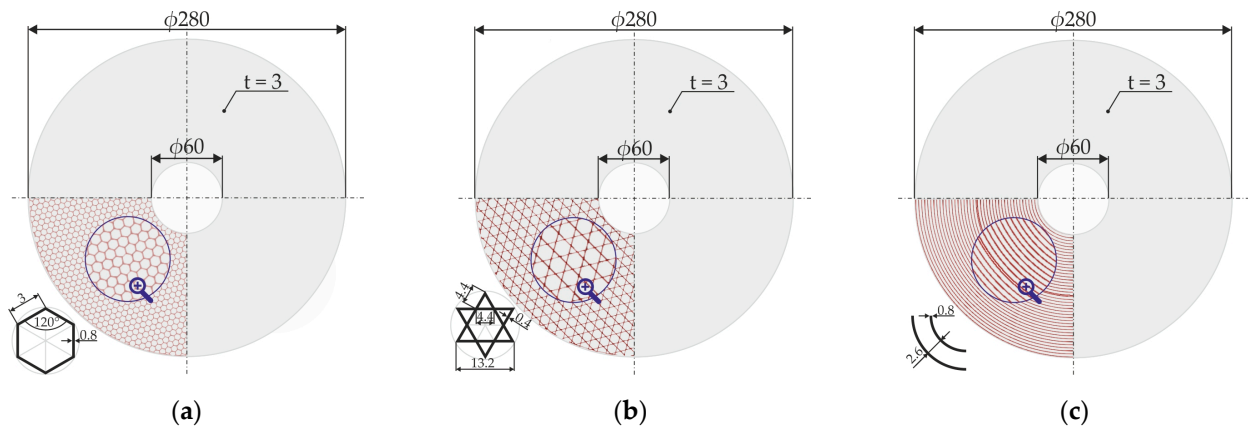


**Figure 1.** Schemes of specimens with part of the top surface showing the infill patterns: (a) honeycomb; (b) stars; (c) concentric.

After the production of specimens (Figure 2a), their weights were measured with a precision digital XS balance, model BL 2002 (Giorgio Bormac s.r.l., Carpi, Italy), with a capacity of 2000 g, division of 0.01 g, and repeatability of 0.01 g (Figure 2b). Each specimen's weight was measured three times, whereby the scale was calibrated before each measurement. The average measured weights of the specimens are presented in Table 2.



**Figure 2.** Experimental chain: (a) manufactured specimen; (b) digital balance; (c) unmounted specimen with the designed fixture put on the robust frame (modal shaker); (d) torque wrench with digital torque adaptor; (e) input module and modal hammer; (f) vibrometer with the specimen prepared for the analysis.

**Table 2.** Measured weights of the analysed specimens.

Infill Pattern	Weight (g)
Honeycomb	151.55
Star	148.49
Concentric	148.42

The specimen dimensions were determined according to the dimensions of the 3D printer's heated table and the requirement to clamp the specimens properly using a designed and manufactured fixture containing four through-holes (Figure 2c), allowing the



bolt connection of the specimen to the robust frame (Figure 2c,f). Bolt tightening was done using a torque wrench with an applied digital torque adapter (Figure 2d).

The excitation of the structure was realized using a Brüel & Kjær 8206 (Hottinger Brüel & Kjær A/S, Virum, Denmark) impact hammer with a plastic tip (Figure 2e). As all the specimens manufactured were made of plastic material, they were very light-weight. The mentioned impact hammer, with an output voltage sensitivity of 22.7 mV/N and full-scale force range compression of 220 N, is suitable for the implementation of impact-force measurements on small to medium structures. The application of a plastic tip allowed us to obtain optimal impulse shapes in the set frequency span. The use of conventional accelerometers to acquire specimens' responses was not possible due to their size, mass, and attachment method, which could cause undesirable mass loading or local stiffness changes. Such an approach could lead to inaccurate measurements of the specimen's true dynamic behaviour, causing mode shape distortion or inaccurate damping measurement. For this reason, the measurement of responses in the form of velocities was realized using a non-contact PDV-100 (Polytec GmbH, Waldbronn, Germany) portable digital vibrometer (Figure 2f) based on the laser Doppler principle. This device is designed to remotely acquire a sample's vibrational velocities in a frequency range from 0.5 Hz up to 22 kHz and provides three measurement ranges for full-scale outputs: 20, 125, and 500 mm/s. Frequency response functions (FRFs), i.e., mobilities, were acquired using the Brüel & Kjær Pulse<sup>®</sup> system with a LAN-XI module type 3050 (Hottinger Brüel & Kjær A/S, Virum, Denmark), containing six high-precision BNC input channels with an input range up to 51.2 kHz. To carry out the measurements, the Pulse MTC Hammer V.21.0.0 software (Hottinger Brüel & Kjær A/S, Virum, Denmark) was used.

The process of modal parameter estimation for the manufactured specimens was carried out in two phases. The first, i.e., the pre-test phase, involved 18 measurements (see Table 3) realized on the specimen with a honeycomb infill pattern. Each of the measurements belonged to a specific stage of the pre-test phase, indicated in Table 3 by the Roman letters I<sup>ref</sup> to IV<sup>F</sup>.

**Table 3.** Settings used in particular stages of experimental modal analysis carried out in the pre-test phase. DOFs = degrees of freedom (excitation points), REF = reference degree(s) of freedom (locations of response measurement), NoM = number of measurements, NoE = number of evaluations.

Stage	Torque (Nm)	DOFs	REFs	Sampling Frequency (Hz)	Analysis Lines	NoM	NoE
I <sup>ref</sup>	6	1 to 48	49	1600	400	3	3
II <sup>A</sup>	6	1 to 24	25	1600	400	3	3
II <sup>B</sup>	6	1 to 96	97	1600	400	3	3
III <sup>A</sup>	6	1 to 48	49	1600	800	3	3
III <sup>B</sup>	6	1 to 48	49	1600	1600	3	3
IV <sup>A</sup>			49, 50, 51				3
IV <sup>B</sup>			49, 50				3
IV <sup>C</sup>			49, 51				3
IV <sup>D</sup>	6	1 to 48	50, 51	1600	400	3	3
IV <sup>E</sup>			51				3
IV <sup>F</sup>			50				3
Total:						18	33

The experimental process realized herein will be explained for the reference measurements (I<sup>ref</sup>), the results of which were then compared with those obtained in the other three stages of this phase. Each experimental estimation of modal parameters started with the clamping of the specimen to the modal shaker armature. As in modal analysis, the tightening of the constraint plays a significant role in determining the stiffness of the system, influencing all the modal parameters analysed (i.e., mode shapes, natural frequencies, and damping ratios); therefore, clamping of the specimen to the armature was ensured by

fixturing with four bolts tightened to the same torque of 6 Nm using a torque wrench with a DMA 40/200D (Dema Vertriebs GmbH, Übrigshausen, Germany) applied digital torque adapter. It should be mentioned that the shaker itself was used in this case just to create the constraint (clamped joint occurring on a small annular area at the top and bottom surfaces of the specimen). However, in the future, it will provide the authors with the possibility to implement modal testing with a different type of excitation.

Subsequently, the necessary analysis settings were defined in MTC Hammer. The settings used in the  $I^{\text{ref}}$  stage were as follows:

- Sensor types definition: definition of the exciter (Brüel & Kjær 8206) and response sensor (PDV-100) types and their assignment to individual channels of the LAN-XI module type 3050 was done;
- Geometric model creation: the planar geometric model of the analysed specimen was created. It consisted of the 48 points of defined coordinates, mutually connected by triangular surfaces (Figure 3);

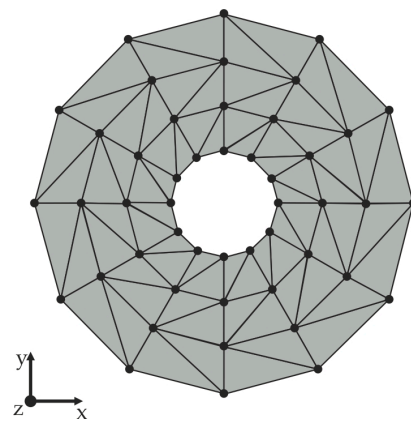


**Figure 3.** A geometric model of the specimen created in the  $I^{\text{ref}}$  stage, containing 48 points and the corresponding number of triangular surfaces.

- Measurement sequence definition: the measurement was planned in the form of the roving hammer-impact method and carried out using the fixed embedded vibrometer, i.e., 48 degrees of freedom (DOFs) representing the excitation points and 1 reference degree of freedom (REF): point 49 for response measurement. Excitations and response measurements were carried out perpendicularly to the specimen's top surface, i.e., in the Z-direction, in all stages of the experimental texting. The blue annular surface in the scheme in Figure 4 corresponds to the clamped part of the specimen surface. The positions of the four bolts were, in each measurement, aligned to the 1-4-7-10 DOFs.

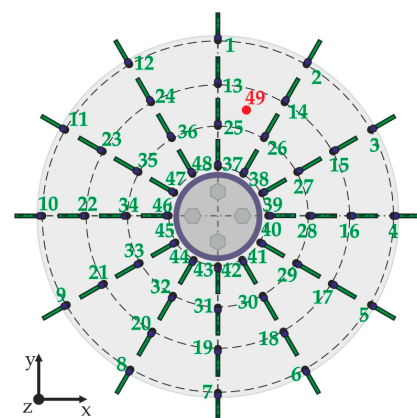


**Figure 4.** Measurement sequence of the specimen analysed in  $I^{\text{ref}}$  analysis containing 48 degrees of freedom and one reference degree of freedom (point 49).

- Frequency span and resolution definition: the sampling frequency set to 1600 Hz allowed analysis of the dynamic behaviour of the specimen in the 0–800 Hz frequency span. The definition of the analysis lines number as equal to 400 ensured the frequency resolution of 2 Hz (acquisition time 500 ms);
- Triggering and weighting of the signals: after defining the proper level of trigger impact signal, and hammer and response weighting, the measurement of the FRFs was started.

Each of the DOFs was excited five times by the impact hammer, and the resulting signals were obtained by averaging using the linear peak hold average method on the fast Fourier transformation (FFT) signals, which should ensure adequate accuracy of the FRFs. The evaluation of FRFs was carried out in Pulse Reflex<sup>®</sup> (Hottinger Brüel & Kjær A/S, Virum, Denmark). Information on the natural frequencies, damping ratios, and mode shapes of the individual modes of oscillation was analysed in the 0–800 Hz frequency span. Stability diagrams resulting from the magnitude of the complex mode indicator function (CMIF) were used to estimate the particular modes. The CMIF is based on singular value decomposition (SVD), has one function for each reference degree of freedom and can be used to detect closely spaced or repeated modes.

To identify the stability of the poles, the rational fraction polynomial-Z method with 40 iterations was used. The selected possible modes were analysed by the automatic modal assurance criterion (auto MAC), which is a method based on orthogonality checking that is used to compare mode shapes and determine the level of similarity between them. It is a very useful tool for the identification of closely spaced modes or repeated modes which have very close or the same frequencies but distinct mode shapes. The so-called MAC value between two mode shape vectors  $\Phi_i$  and  $\Phi_j$  is calculated according to:

$$\text{MAC}(\Phi_i, \Phi_j) = \frac{|\Phi_i^T \Phi_j|^2}{(\Phi_i^T \Phi_i)(\Phi_j^T \Phi_j)} \quad (1)$$

The resulting matrix, with the rows and columns representing the mode shapes, has diagonal elements equal to 1 and off-diagonal elements which provide information about the correlation between selected mode shapes. A MAC value equal to 1 represents identical mode shapes, while a MAC value equal to 0 corresponds to completely distinct mode shapes.

After completion of the measurement, the specimen was unmounted. Subsequently, the specimen was clamped again and the above-described process (without geometry definition, which can be imported) of modal analysis was repeated another two times. The results obtained from each set of three measurements were averaged to ensure the proper graphical and quantitative comparison of the modal parameters. The pre-test phase was designed to analyse the influence of the selected parameters, i.e., the number of degrees of freedom (DOFs), the number of analysis lines, and the number and location of reference degrees of freedom (REFs) on the modal parameters of the specimen with a honeycomb infill pattern. The measurement sequences, DOFs, and REFs considered for the pre-test stages I<sup>ref</sup> up to V<sup>F</sup> (according to Table 3) are shown in Figure 5.

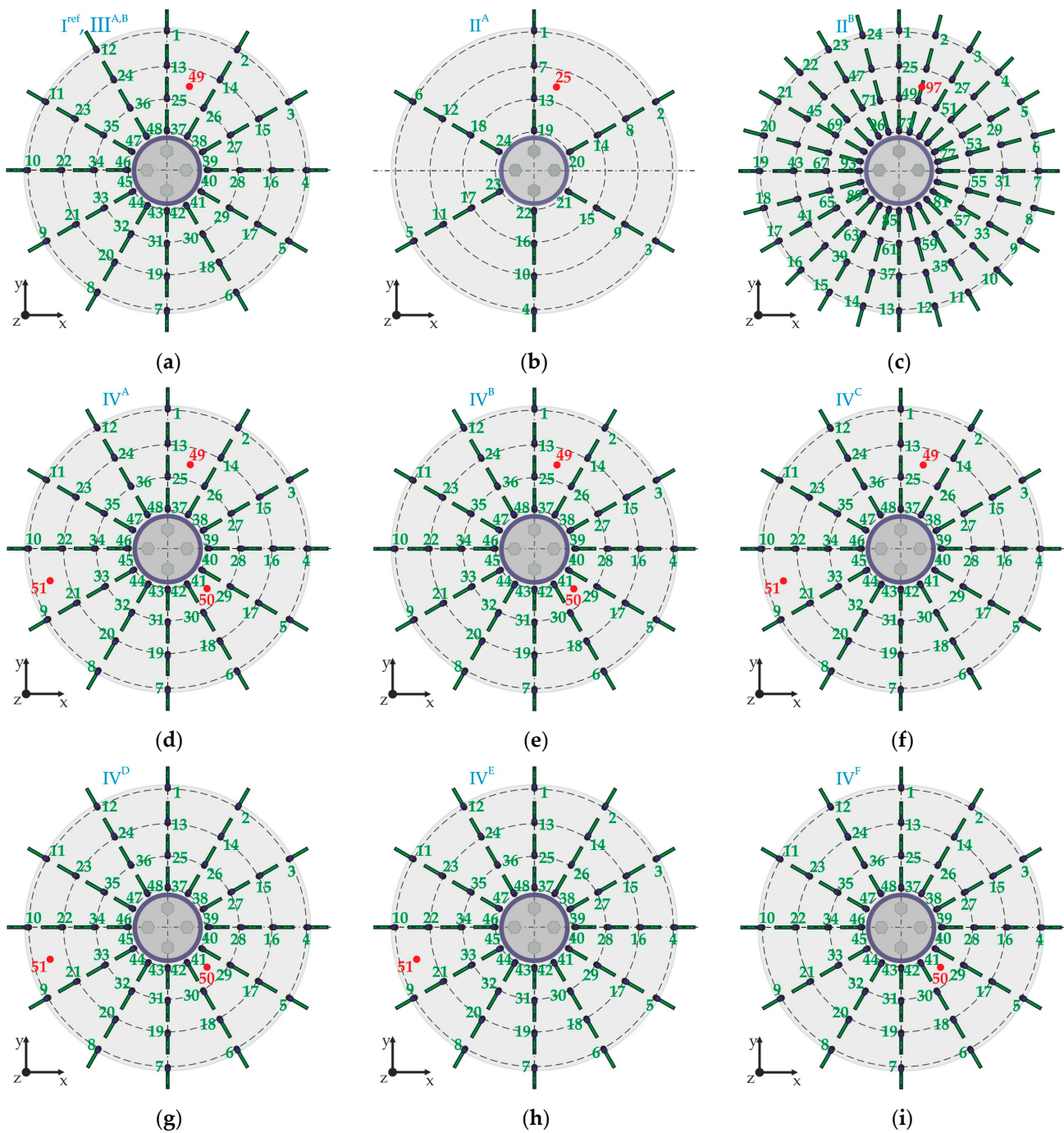


**Figure 5.** Measurement sequences containing DOF and REF of the specimen with honeycomb infill pattern analysed in the: (a)  $I^{ref}$  and  $III^{A,B}$ ; (b)  $II^A$ ; (c)  $II^B$ ; (d)  $IV^A$ ; (e)  $IV^B$ ; (f)  $IV^C$ ; (g)  $IV^D$ ; (h)  $IV^E$ ; and (i)  $IV^F$  stages of the pre-test phase.

### 3. Results

#### 3.1. Realization and Evaluation of the Pre-Test Phase

##### 3.1.1. Results Obtained in the $I^{ref}$ Stage of the Pre-Test Phase

As mentioned in Section 2, the  $I^{ref}$  stage consists of the realization of three modal tests and subsequent estimations of the modal parameters due to the CMIFs corresponding to the singular value decomposition of FRFs. The plots of the CMIFs, shown in Figure 6, indicate good agreement between the results of the realized modal tests.



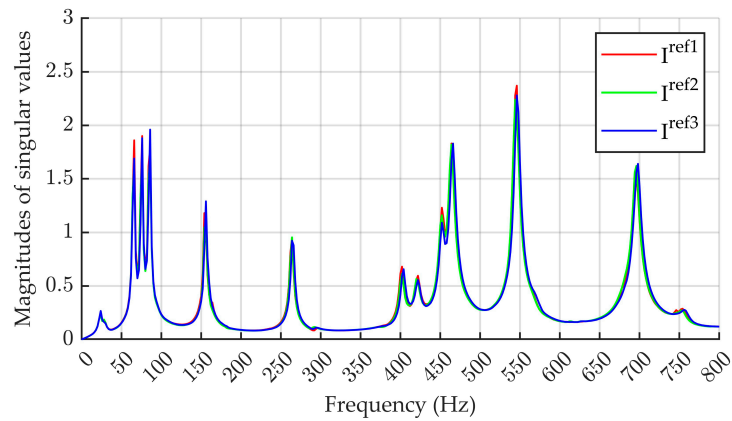


**Figure 6.** Singular curves of CMIF plots obtained from the three experimental modal analyses carried out in the reference  $I^{ref}$  stage of the pre-test phase.

Two peaks around 23 Hz and 27 Hz correspond to the rigid modes (rigid translation in the Z-axis direction and rigid rotation around the Y-axis) caused by the clamping of the specimen to the modal shaker. Since the mode corresponding to the peak around 757 Hz exhibited a high complexity (approximately 0.9), the authors assume that this is not the true mode of the analysed specimen. The result of the analysis of possible modes using the auto MAC from the  $I^{ref1}$  measurement is shown in Figure 7. As all the off-diagonal elements are represented by very small numbers approaching zero, the analysis that we carried out led to the estimation of 11 modes which are well separated in frequency.

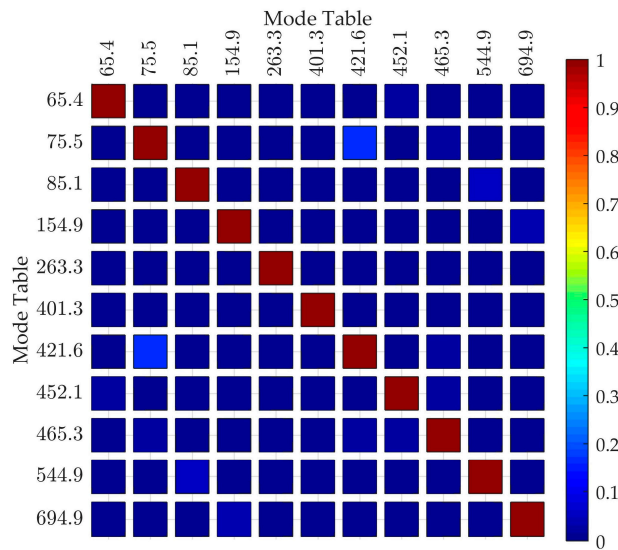


**Figure 7.** The analysis of the possible modes from the  $I^{ref1}$  measurement using auto MAC.

The estimated natural frequencies (presented with precision of one decimal point) and damping ratios (presented with precision of three decimal points) of particular modes are presented in Tables 4 and 5.

The mean course of the CMIF as well as the mean values of both the natural frequencies and damping ratios (lines denoted in Tables 4 and 5 as  $I^{ref}$  (mean)), respectively, were further used for comparison with the results obtained in the following stages of the pre-test phase. The mode shapes corresponding to the particular modes are shown in Figure 8.

**Table 4.** Natural frequencies of the clamped specimen with a honeycomb infill pattern estimated in the I<sup>ref</sup> stage of the pre-test phase.

Stage	Estimated Natural Frequencies (Hz)										
	Mode 1	Mode 2	Mode 3	Mode 4	Mode 5	Mode 6	Mode 7	Mode 8	Mode 9	Mode 10	Mode 11
I <sup>ref</sup> 1	65.4	75.5	85.1	154.9	263.3	401.3	421.6	452.1	465.3	544.9	694.9
I <sup>ref</sup> 2	65.2	75.4	85.2	155.2	263.5	401.4	420.8	451.3	464.5	544.5	695.0
I <sup>ref</sup> 3	65.4	75.7	85.6	156.0	264.8	403.3	422.1	452.1	466.2	546.0	696.9
I <sup>ref</sup> (mean)	65.3	75.5	85.3	155.4	263.9	402.0	421.5	451.8	465.3	545.1	695.6

**Table 5.** Damping ratios of the clamped specimen with a honeycomb infill pattern estimated in the I<sup>ref</sup> stage of the pre-test phase.

Stage	Estimated Damping Ratios (%)										
	Mode 1	Mode 2	Mode 3	Mode 4	Mode 5	Mode 6	Mode 7	Mode 8	Mode 9	Mode 10	Mode 11
I <sup>ref</sup> 1	1.448	1.440	1.262	0.879	0.712	0.618	0.771	0.586	0.699	0.559	0.605
I <sup>ref</sup> 2	1.418	1.425	1.206	0.794	0.697	0.601	0.728	0.648	0.739	0.554	0.584
I <sup>ref</sup> 3	1.514	1.431	1.257	0.851	0.710	0.613	0.784	0.657	0.733	0.558	0.572
I <sup>ref</sup> (mean)	1.460	1.432	1.242	0.841	0.706	0.611	0.761	0.630	0.724	0.557	0.587

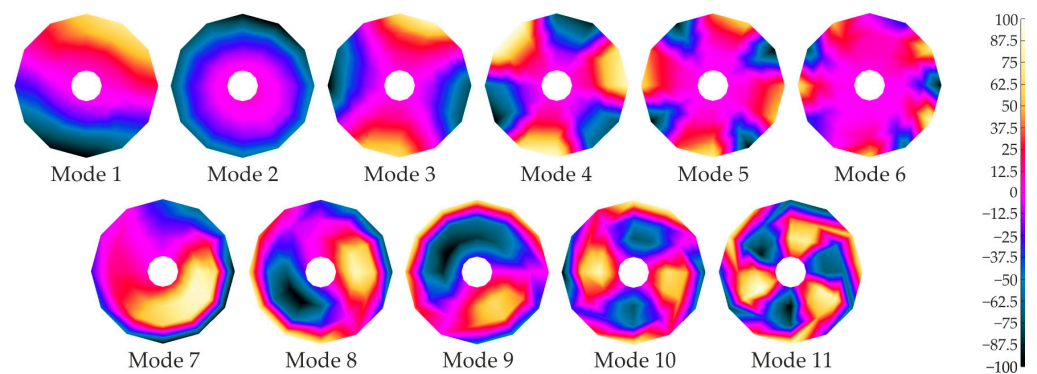


**Figure 8.** Mode shapes of the clamped specimen with honeycomb infill pattern estimated in the I<sup>ref</sup> stage (model with 48 DOFs) of the pre-test phase.

### 3.1.2. Results Obtained in the II Stage of the Pre-Test Phase

This stage of the pre-test phase was intended to analyse the possibility of reducing the time requirements for the measurement by reducing the number of DOFs. Since the aim of the authors was to compare the modal parameters of all three specimens with different infill patterns, estimated from a larger amount of repeated measurements, reducing the DOF number to, e.g., 50% (i.e., 24) would lead to considerable time-saving. On the other hand, if the results of analyses with a larger DOF number (i.e., 96) would lead to significant changes in the mode shapes or the analysed modal parameters (natural frequencies and damping ratios), the authors would already have the possibility of making the required adjustments to increase the accuracy of the analysis at this pre-test phase.

When comparing the mean courses of the CMIFs (Figure 9) obtained from the three measurements realized in both the I<sup>ref</sup> and II stages, the plots were found to be vertically shifted compared to each other. In addition, significant differences in the heights of the individual CMIF peaks can be seen. The authors consider that the above differences in the plots are related to the fact that the accuracy of the singular value decomposition depends on employing a sufficient number of DOFs to capture the responses of all structure modes.

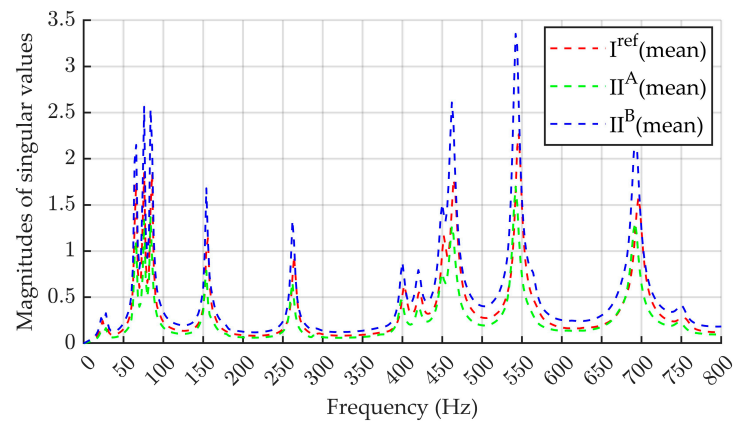


**Figure 9.** Comparison of mean singular curves of CMIF plots obtained from the three experimental modal analyses carried out in the  $I^{\text{ref}}$ ,  $II^{\text{A}}$ , and  $II^{\text{B}}$  stages of the pre-test phase.

The abovementioned statement can also be proved through Figure 10, which shows the mode shapes of the model with 24 DOFs. Although most of the mode shapes correspond to those obtained in the  $I^{\text{ref}}$  stage, crucial differences can be observed, especially in modes 5 and 6, where the lack of DOFs (too large a distance between excitation points) resulted in an incorrect estimation of the mode shapes.

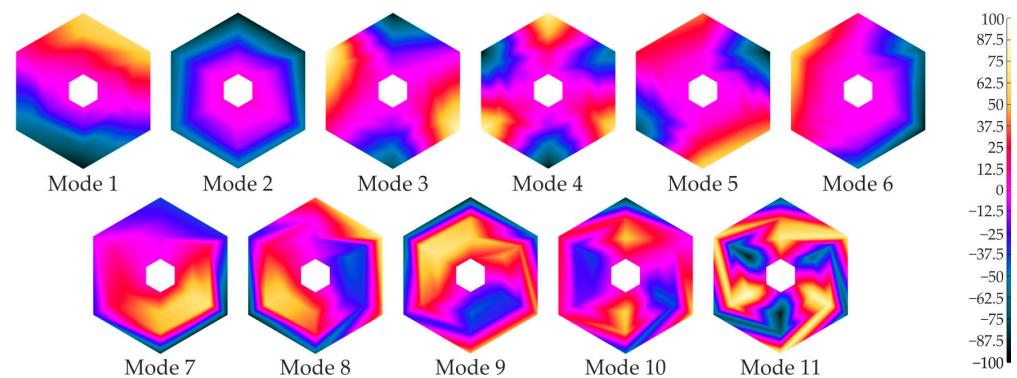


**Figure 10.** Mode shapes of the clamped specimen with honeycomb infill pattern estimated in the  $II^{\text{A}}$  stage (model with 24 DOFs) of the pre-test phase.

The mode shapes depicted in Figure 11 were obtained from the EMA carried out using the model with 96 DOFs, and it is evident that they look smoother than those shown in Figure 8 (obtained for the model with 48 DOFs). On the other hand, it should be noted that the increase in the DOF number increased the time requirements for the realization of the experiments. Based on the comparison of the obtained mode shapes (having the same character as those obtained in the  $I^{\text{ref}}$  stage) and the analysed modal parameters (presented in Section 3.2), this process did not cause significant changes and, thus, the authors consider it necessary to perform an increase in the number of DOFs only in cases when the most accurate mode shape, as the output of the EMA, is required (e.g., for damage identification processes [40]).

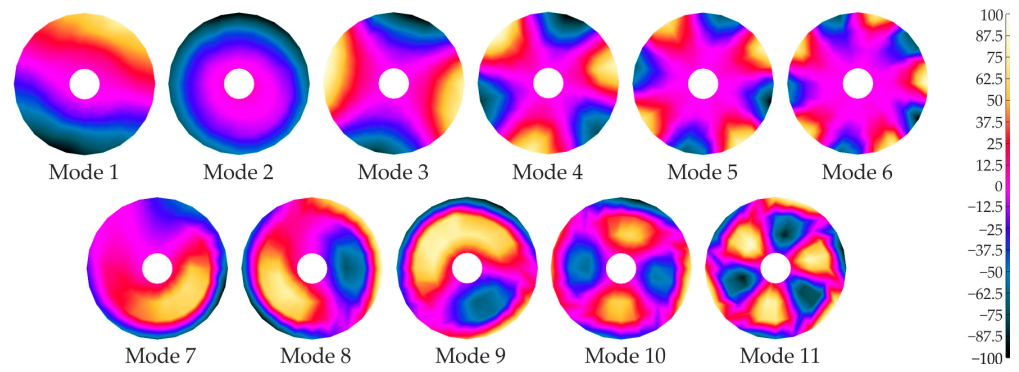


**Figure 11.** Mode shapes of the clamped specimen with honeycomb infill pattern evaluated in the II<sup>B</sup> stage (model with 96 DOFs) of the pre-test phase.

### 3.1.3. Results Obtained in the III Stage of the Pre-Test Phase

The number of analysis lines in an analysed signal defines the balance between the time and frequency resolution and influences the process of performing FFT. A larger number of analysis lines improves the resolution of the frequency domain, as the frequency spectrum is divided into smaller bins. On the other hand, a larger number also increases the time window, i.e., the duration of the signal being transformed, computation time, and memory usage.

Analyses of the symmetric structure with repeated modes near the same frequency or closely spaced modes, where a high-resolution FFT is required to separate them, can be a reason for using a larger number of analysis lines. The MTC Hammer V21.0.0 software, using which the EMAs described in this article were carried out, allows the user to set the frequency span  $F_s$  and the number of analysis lines  $N$ . The frequency resolution  $df$  and block length  $T$  are then calculated as follows:

$$df = \frac{F_s}{N}, \tag{2}$$

$$T = \frac{1}{F_s}. \tag{3}$$

This stage of the pre-test phase is intended to analyse the modal parameters obtained for three different numbers of analysis lines, i.e.,  $N = 400$  (set in the I<sup>ref</sup> stage),  $N = 800$  (set in the III<sup>A</sup> stage), and  $N = 1600$  (set in the III<sup>B</sup> stage). As the same 0–800 Hz frequency span was set in each of the measurement stages, it led to changes in the frequency resolution from 2 Hz to 1 Hz and finally to 0.5 Hz. The mean courses of the CMIF plots obtained from the three measurements realized in the I<sup>ref</sup>, III<sup>A</sup>, and III<sup>B</sup> stages can be seen in Figure 12.

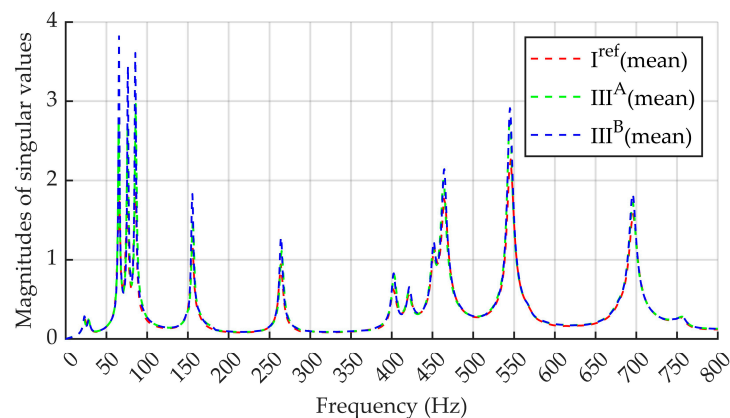


**Figure 12.** Comparison of mean singular curves of CMIF plots obtained from the three experimental modal analyses carried out in the I<sup>ref</sup>, III<sup>A</sup>, and III<sup>B</sup> stages of the pre-test phase.



In contrast to the courses from the second stage of the pre-test phase, in this case, it is not possible to observe the mutual vertical shift of the singular lines. However, it is obvious that the larger the number of analysis lines, the higher, sharper, and narrower the CMIF peaks. Since the damping ratio is estimated based on the width of the resonance peaks, narrower peaks can lead to an underestimation of the damping ratios. Moreover, in each measurement realized, an exponential weighting of the response was used. The combination of a higher frequency resolution with exponential weighting of the responses leads in general to a minimization of the spectral leakage. Such a reduction in leakage contributes to the sharpness of the peaks as well, resulting in a lower damping ratio. Although there was no change observed in the natural frequencies, a significant decrease in the damping ratio was obtained, especially for the first five modes (see the quantitative comparison of the results in Section 3.2). No new or closely spaced modes were found in this measurement stage. The estimated mode shapes look the same as those from the  $I^{\text{ref}}$  stage.

#### 3.1.4. Results Obtained in the IV Stage of the Pre-Test Phase

In structures with geometric or material symmetry, so-called repeated modes commonly arise as a consequence of the symmetry in the structure's stiffness and mass distribution. It is characteristic of repeated modes that they occur at the same or nearly the same natural frequency, but correspond to distinct (mathematically orthogonal) mode shapes. As these modes share the same frequency, identifying repeated modes can be difficult. The CMIF is one of the functions used for the identification of repeated modes. In the previously mentioned measurements, repeated modes were not identified. The reason for this is that only one reference degree of freedom was used to capture the responses of the specimen and, thus, the CMIF plot consists of only one singular curve. However, modes that might appear as a single peak in a single-reference CMIF plot may split into distinct peaks in a multi-reference setup. If the measurement is carried out in a multiple input, multiple output (MIMO) form, the result is a graphical plot containing the same number of singular curves as the number of reference degrees of freedom used to capture the response.

To analyse the effect of the chosen position of the reference degree of freedom, three multi-reference measurements were realized. Since the authors' workplace possesses only one Polytec PDV-100 vibrometer, the implementation of the MIMO measurements was carried out in the following way. The measurement sequence consisted of three parts. Firstly, the excitation of the specimen was realized using the roving hammer-impact method in 48 DOFs with the responses being captured by a fixed embedded vibrometer located in reference degree of freedom 49 (the same process as in the  $I^{\text{ref}}$  stage). Subsequently, the position of the vibrometer was changed to the location of reference degree of freedom 50 and the same 48 DOFs were excited by the roving hammer. Finally, the same process was implemented after changing the vibrometer position to the location of reference degree of freedom 51 (see the locations of reference degrees of freedom in Figure 5). However, these measurements were evaluated separately with different amounts of obtained FRFs depending on the number and location of the selected reference degree(s) of freedom (according to column 4 of Table 3 and Figure 5d–i, respectively). Such measurements and evaluations were aimed to highlight the fact that inappropriately chosen positions of the reference degrees of freedom can affect the results of the analyses in such a way that not every mode will be detected. On the other hand, an appropriately chosen larger number of reference degrees of freedom allows one to obtain information not only about repeated modes but also about closely spaced modes that may not have been identified in the previous three stages.

As the number of singular curves obtained from the SVD of the FRFs corresponds to the number of reference degrees of freedom, three singular curves were obtained in each measurement evaluated in the  $IV^A$  stage. Similarly, two singular curves represented the output from the SVD realized in stages  $IV^B$  to  $IV^D$  and only one singular curve corresponded to each measurement of the  $IV^E$  and  $IV^F$  stages of the pre-test phase. The plots of the mean

singular curves obtained from the three measurements realized in stages IV<sup>A</sup> to IV<sup>D</sup> can be seen in Figure 13, whereby the same representation of y-axis limits was used for better visual comparison of the singular values' magnitudes. Each of the singular curves captures different aspects of the specimens' modal behaviour, i.e., the modes that are poorly captured by one reference degree of freedom can be better captured by another.

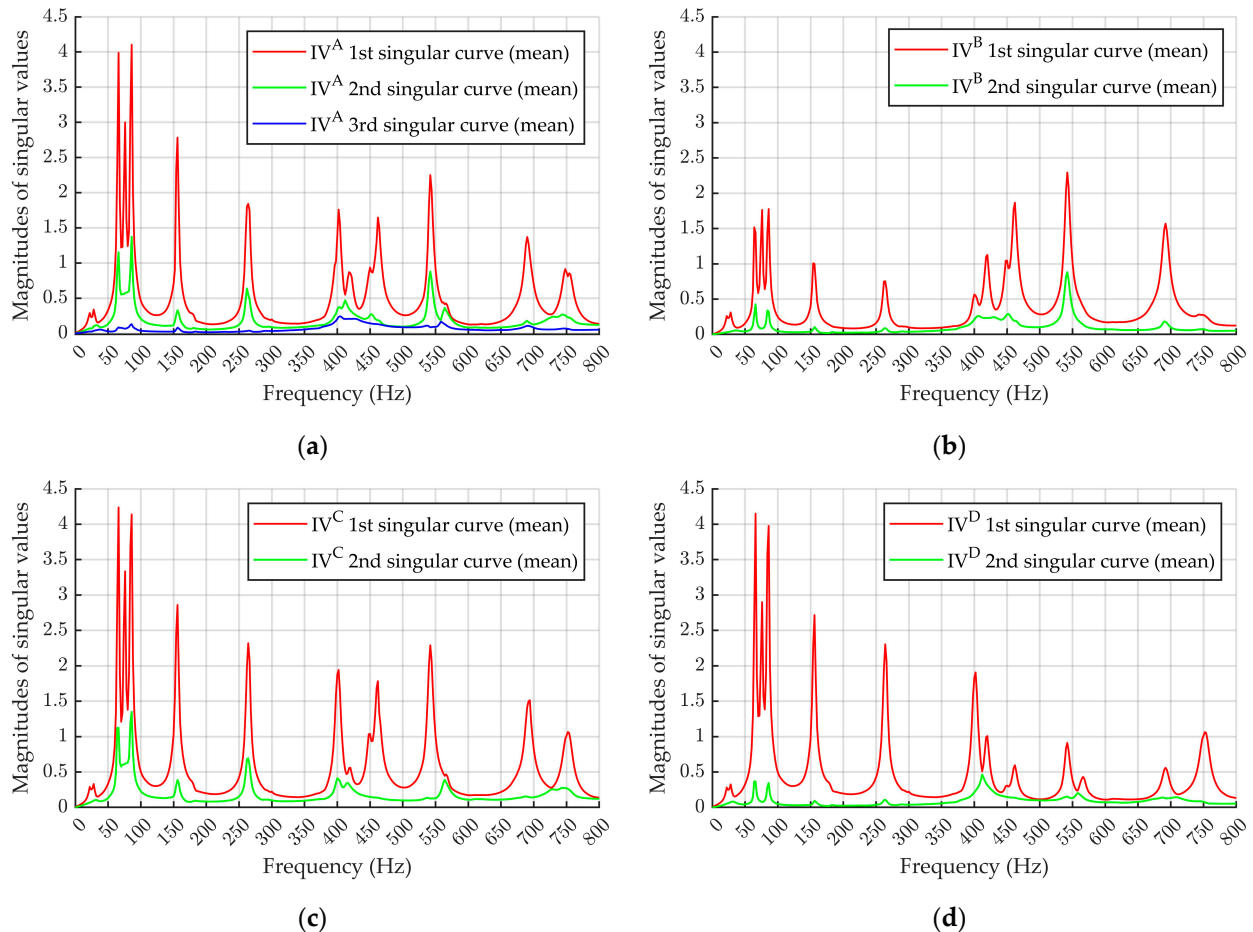


**Figure 13.** Mean singular curves of the CMIF plots obtained from three measurements in the: (a) IV<sup>A</sup>; (b) IV<sup>B</sup>; (c) IV<sup>C</sup>; and (d) IV<sup>D</sup> stages of the pre-test phase.

Comparing the CMIF plots, it is obvious that each combination of reference degrees of freedom used in the MIMO measurements contributes to the magnitudes of singular values differently. For example, the magnitudes of the first singular curve in Figure 13b are much smaller than in the other cases. Moreover, repeated modes appear in the CMIF plot as peaks in multiple singular curves at the same (or very close) frequency, which is not evident in each of the realized cases (see the comparative table of assessed modes presented in Section 3.2). The auto MAC was used to correlate the similarities between the modes with an emphasis on proving that some of the selected modes with closely spaced natural frequencies are the repeated modes. The off-diagonal elements of the MAC matrix shown in Figure 14 include mainly the values from 0 to 0.2 (only one value is approaching 0.3). This indicates that the modes, estimated in one of the IV<sup>A</sup> stage measurements, share very close frequencies and have distinct mode shapes, i.e., they are repeated.

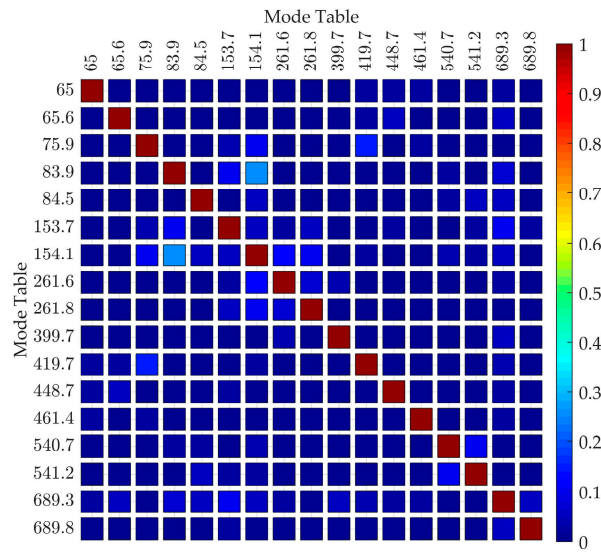


**Figure 14.** Possible modes analysis using auto MAC realized in one of the IV<sup>A</sup> stage measurements.

The mode shapes estimated as repeated modes can be seen in Figure 15 labelled by Greek symbols  $\alpha$  and  $\beta$ . Moreover, as the specimen response was captured from multiple points, the obtained singular curves contain richer mode shape information, leading to a more accurate and detailed reconstruction of the mode shapes.

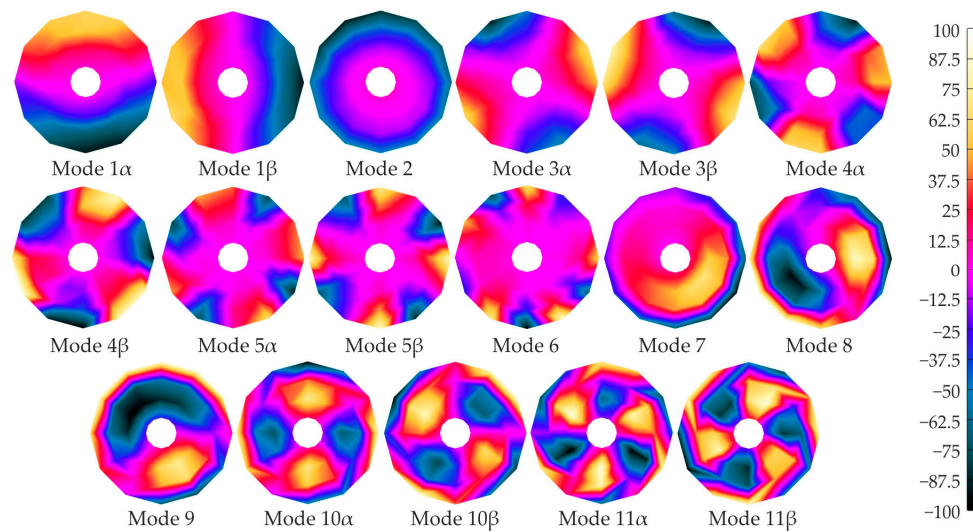


**Figure 15.** Mode shapes of the clamped specimen with a honeycomb infill pattern estimated in stage IV<sup>A</sup> of the pre-test phase. Indices  $\alpha$  and  $\beta$  represent the repeated modes.

In contrast to Figure 13, where the CMIF plots consisted of three and two singular curves, respectively, Figure 16 shows a comparison of the particular mean singular curves of the CMIF plots obtained when evaluating the EMAs conducted with three different locations of the reference degree of freedom, i.e., 49, 50, and 51, respectively. It is obvious that the singular curves obtained in the I<sup>ref</sup>, IV<sup>E</sup>, and IV<sup>F</sup> stages are significantly different. When using reference degrees of freedom 50 and 51, some modes of the analysed specimen with a honeycomb infill pattern were not found (see the comparative table of estimated modes presented in Section 3.2).

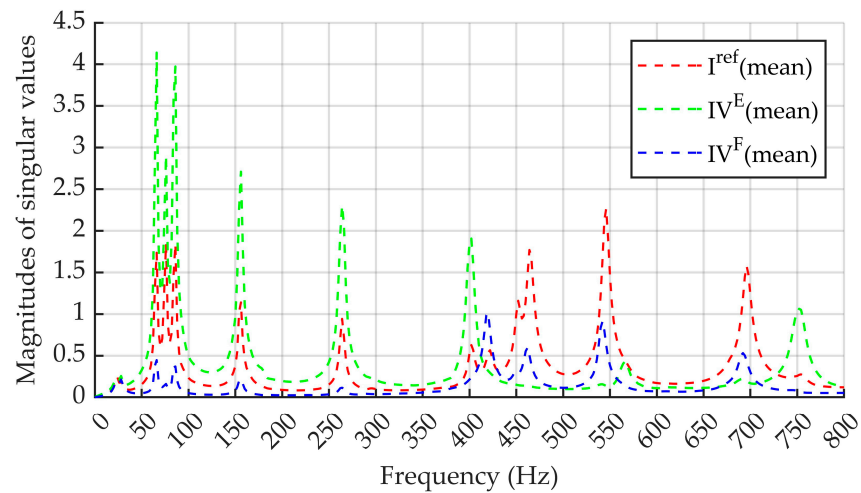


**Figure 16.** Comparison of mean courses of CMIF plots obtained from the three experimental modal analyses carried out in the  $I^{ref}$ ,  $IV^E$ , and  $IV^F$  stages of the pre-test phase.

3.2. Comparison of the Results Obtained in the Pre-Test Phase

The following tables, Tables 6 and 7, present the mean values of the natural frequencies and damping ratios corresponding to individual modes estimated in the previously mentioned stages of the pre-test phase. It can be concluded that, in the case of the analysed honeycomb infill pattern specimen, 11 modes were detected in the selected 0–800 Hz frequency span. Since the specimen is geometrically symmetric, in the case of the realization of multi-reference measurement, information about the repeated modes and their corresponding frequencies or damping ratios was obtained. It should also be mentioned that not all of the above-mentioned modes of the specimen were found in the stages when the structure response measurements were performed at reference degree of freedom locations 50 and 51, respectively ( $IV^C$  to  $IV^F$  stages).

**Table 6.** Natural frequencies of the clamped specimen with a honeycomb infill pattern estimated in the pre-test phase.  $\alpha$ ,  $\beta$  = repeated modes, † = mode was not found.

Stage	Estimated Natural Frequency (Hz)											MVRD
	Mode 1	Mode 2	Mode 3	Mode 4	Mode 5	Mode 6	Mode 7	Mode 8	Mode 9	Mode 10	Mode 11	
$I^{ref}$ (mean)	65.3	75.5	85.3	155.4	263.9	402.0	421.5	451.8	465.3	545.1	695.6	----
$II^A$ (mean)	65.2	75.9	84.4	153.8	261.6	398.9	420.1	449.3	463.0	541.7	690.7	0.65%
$II^B$ (mean)	65.1	75.6	84.7	154.4	262.3	399.6	420.1	449.3	463.0	542.3	691.7	0.49%
$III^A$ (mean)	65.2	76.0	85.9	156.3	264.7	402.7	420.7	450.7	464.1	544.3	694.8	0.32%
$III^B$ (mean)	65.4	76.3	85.4	155.5	264.1	402.3	421.7	451.3	464.9	544.7	694.9	0.08%
$IV^A$ (mean)	64.9 $\alpha$	75.5	84.9 $\alpha$	155.7 $\alpha$	263.3 $\alpha$	401.8	419.3	448.9	462.0	541.6 $\alpha$	691.2 $\alpha$	0.43%
	65.5 $\beta$		85.5 $\beta$	155.8 $\beta$	264.0 $\beta$					541.9 $\beta$	691.8 $\beta$	0.35%
$IV^B$ (mean)	64.9 $\alpha$	75.5	84.9 $\alpha$	155.4 $\alpha$	263.3 $\alpha$	401.8	419.3	448.9	462.0	541.5 $\alpha$	691.1 $\alpha$	0.41%
	65.5 $\beta$		85.4 $\beta$	155.5 $\beta$	264.0 $\beta$					541.9 $\beta$	691.4 $\beta$	0.36%
$IV^C$ (mean)	64.9 $\alpha$	75.5	84.9 $\alpha$	155.2 $\alpha$	263.3 $\alpha$	402.4	419.1	448.8	462.1	541.8 $\alpha$	691.2 $\alpha$	0.42%
	65.5 $\beta$		85.4 $\beta$	156.0 $\beta$	264.3 $\beta$					†	†	0.33%
$IV^D$ (mean)	64.9 $\alpha$	75.5	84.9 $\alpha$	155.2 $\alpha$	263.4 $\alpha$	401.7	419.2	448.9	462.1	541.9 $\alpha$	691.1 $\alpha$	0.41%
	65.5 $\beta$		85.5 $\beta$	155.6 $\beta$	264.0 $\beta$					†	†	0.29%
$IV^E$ (mean)	65.4	75.5	85.1	155.6	263.7	401.6	†	†	†	542.6	691.7	0.21%
$IV^F$ (mean)	65.2	†	85.1	155.6	263.7	†	419.2	448.9	462.1	541.9	691.4	0.41%



**Table 7.** Damping ratios of the clamped specimen with a honeycomb infill pattern estimated in the pre-test phase.  $\alpha, \beta$  = repeated modes, † = mode was not found.

Stage	Estimated Damping Ratio (%)											MVRD
	Mode 1	Mode 2	Mode 3	Mode 4	Mode 5	Mode 6	Mode 7	Mode 8	Mode 9	Mode 10	Mode 11	
I <sup>ref</sup>	1.460	1.432	1.242	0.841	0.706	0.611	0.761	0.630	0.724	0.557	0.587	----
II <sup>A</sup>	1.461	1.426	1.289	0.914	0.742	0.630	0.778	0.654	0.744	0.568	0.579	3.03%
II <sup>B</sup>	1.459	1.448	1.277	0.900	0.723	0.624	0.785	0.635	0.722	0.567	0.585	1.99%
III <sup>A</sup>	1.018	1.050	0.893	0.617	0.598	0.548	0.684	0.543	0.672	0.514	0.558	16.46%
III <sup>B</sup>	0.785	0.820	0.702	0.576	0.543	0.541	0.661	0.540	0.634	0.500	0.519	19.77%
IV <sup>A</sup>	1.575 $\alpha$	1.369	1.272 $\alpha$	0.948 $\alpha$	0.729 $\alpha$	0.612	0.775	0.673	0.684	0.627 $\alpha$	0.633 $\alpha$	5.95%
	1.505 $\beta$		1.307 $\beta$	0.860 $\beta$	0.720 $\beta$					0.601 $\beta$	0.600 $\beta$	3.77%
IV <sup>B</sup>	1.571 $\alpha$	1.445	1.260 $\alpha$	0.932 $\alpha$	0.748 $\alpha$	0.630	0.786	0.685	0.687	0.585 $\alpha$	0.611 $\alpha$	5.10%
	1.506 $\beta$		1.273 $\beta$	0.882 $\beta$	0.719 $\beta$					0.573 $\beta$	0.592 $\beta$	3.41%
IV <sup>C</sup>	1.510 $\alpha$	1.404	1.214 $\alpha$	0.883 $\alpha$	0.735 $\alpha$	0.668	0.783	0.628	0.779	0.581 $\alpha$	0.630 $\alpha$	4.41%
	1.487 $\beta$		1.238 $\beta$	0.741 $\beta$	0.724 $\beta$					†	†	4.30%
IV <sup>D</sup>	1.562 $\alpha$	1.369	1.250 $\alpha$	0.914 $\alpha$	0.727 $\alpha$	0.635	0.766	0.649	0.817	0.553 $\alpha$	0.626 $\alpha$	4.68%
	1.502 $\beta$		1.286 $\beta$	0.888 $\beta$	0.721 $\beta$					†	†	3.89%
IV <sup>E</sup>	1.440	1.399	1.270	0.865	0.720	0.613	†	†	†	0.529	0.575	2.27%
IV <sup>F</sup>	1.506	†	1.267	0.854	0.701	†	0.769	0.646	0.827	0.560	0.590	2.92%

Moreover, the tables contain information about the mean value of the relative difference (MVRD) calculated concerning the modal parameters obtained in the I<sup>ref</sup> stage using:

$$MVRD = \frac{1}{n} \sum_{i=1}^n \left| \frac{q^i - q^{ref}}{q^{ref}} \right| 100\%, \tag{4}$$

where  $n$  corresponds to the number of modes found,  $q^i$  represents the value of the compared modal parameter (either natural frequency or damping ratio) estimated in the  $i^{th}$  stage of the pre-test, and  $q^{ref}$  is the value of the compared modal parameter obtained in the I<sup>ref</sup> stage of the pre-test. As some modes were not found in the IV stage, the  $n$  number used in Equation (4) for the calculation of the MVRD has various values ( $n = 11, n = 9,$  or  $n = 8$  depending on the number of modes found).

When comparing the values of the estimated natural frequencies, it can be concluded that the results obtained in all stages of the pre-test phase differed minimally (mean value of relative difference varies from 0.08% up to 0.65%). The maximum MVRD (0.65%) was obtained in the II<sup>A</sup> stage, where the number of excitation points was reduced.

The maximum MVRDs (16.46% and even 19.77%) in the estimated damping ratios were obtained in the III stage of the pre-test. The larger values of analysis lines, set in this stage, caused narrower and sharper peaks to appear in the CMIF plots, leading to the underestimation of the damping ratios. In other cases, the MVRDs were in a range from 2.27% up to 5.95%, which is acceptable for the low values of damping ratios obtained.

### 3.3. Realization and Evaluation of the Second Phase

The aim of the authors in the pre-test phase was to analyse the effects of different settings on the results of the modal analyses to find settings under which comparative measurements of the modal parameters of three shape-, dimension- and mass-correlated circular plates with different infill patterns produced by the FDM method could be carried out. For the experimental conditions, the following was required:

- Realization of the experiments under the same conditions to minimize their influence on the values of the estimated modal parameters;
- Time efficiency in performing a larger series of measurements;
- Sufficient accuracy of the obtained measurement results.

Based on the analysis of the results and time requirements of the individual stages of the pre-test phase, the authors decided to implement the comparative EMAs under the conditions presented in Table 8. The specimen fixture, hardware, and software means of the measurement chain were the same as in the pre-test phase.

**Table 8.** Settings used in the second (comparative) phase of tested specimens’ modal parameters. H = honeycomb, S = star, C = concentric, DOFs = degrees of freedom (excitation points), REF = reference degree of freedom (locations of response measurements), NoM = number of measurements, NoE = number of evaluations.

Measurement	Torque (Nm)	DOF	REF	Sampling Frequency (Hz)	Analysis Lines	NoM	NoE
$\Gamma^{ref1-3} \& H^j$ (for $j = 4$ to 10)	6	1 to 48	49	1600	400	10	10
$S^k$ (for $k = 1$ to 10)	6	1 to 48	49	1600	400	10	10
$C^k$ (for $k = 1$ to 10)	6	1 to 48	49	1600	400	10	10
Total:						30	30

To validate the results, the measurements were realized 10 times. Within each measurement, FRF plots (one example for each specimen can be seen in Figures 17a, 18a and 19a) were obtained, from which CMIF plots (Figures 17b, 18b and 19b) were extracted using SVD.

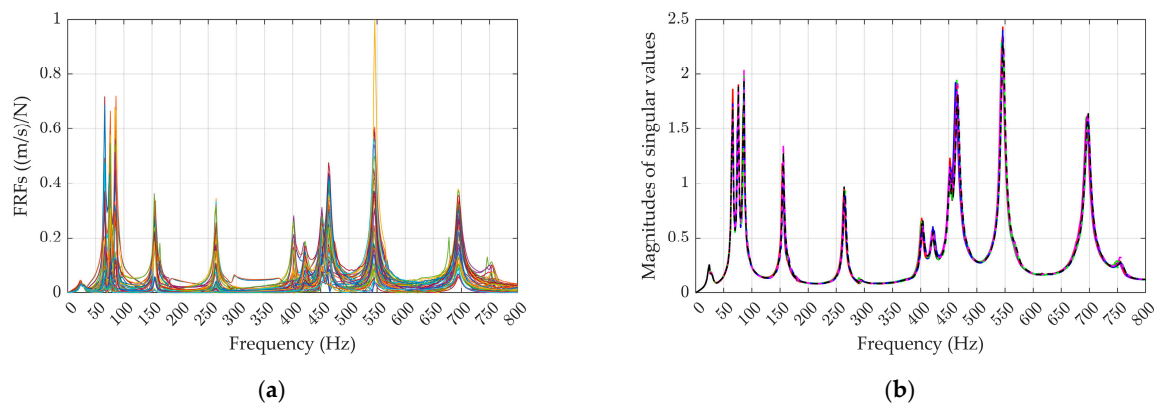


**Figure 17.** Plots of the analysed specimen with honeycomb infill pattern: (a) FRFs obtained from one of the measurements realized; (b) CMIFs obtained from the 10 measurements realized.

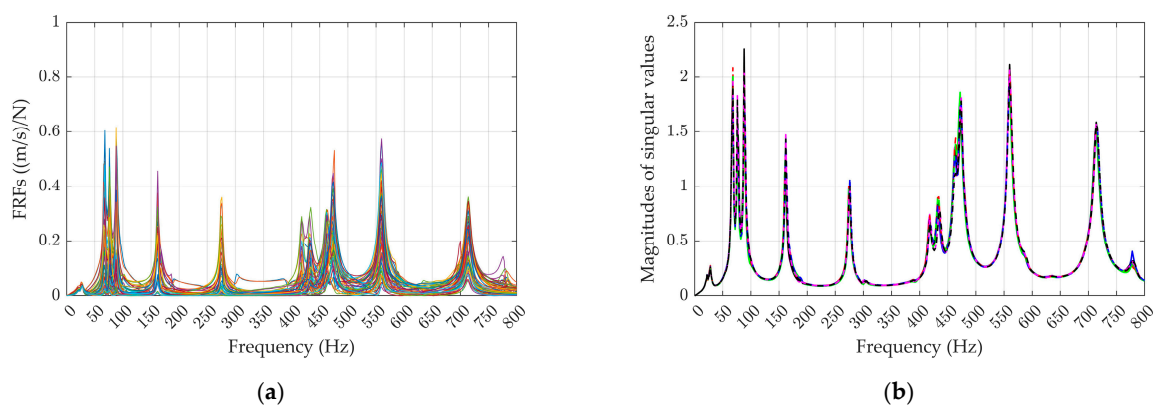


**Figure 18.** Plots of the analysed specimen with star infill pattern: (a) FRFs obtained from one of the measurements realized; (b) CMIFs obtained from the 10 measurements realized.

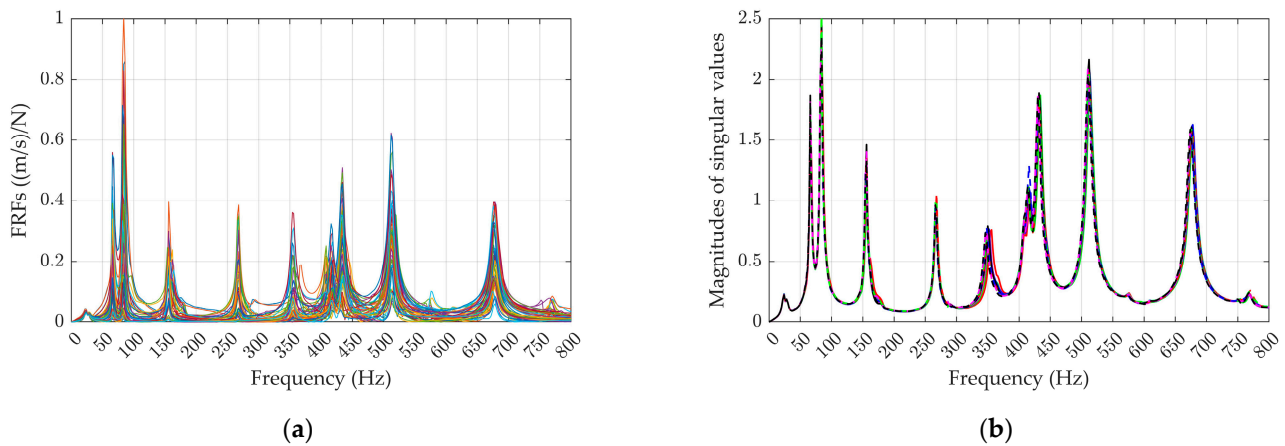


**Figure 19.** Plots of the analysed specimen with concentric infill pattern: (a) FRFs obtained from one of the measurements realized; (b) CMIFs obtained from the 10 measurements realized.

As can be seen from the CMIF plots, very good agreement was obtained in each of the measurements performed. Thus, the results from the measurements are not affected by any outliers and the data represent the true behaviour of the analysed specimens. The mean values of the natural frequencies and damping ratios, estimated using the rational fraction polynomial-Z method with 40 iterations, together with the standard deviations that were calculated, are shown in Tables 9 and 10.

**Table 9.** Mean values of estimated natural frequencies and standard deviations calculated from 10 modal tests of the analysed clamped specimens with different infill patterns. † = mode was not found.

Infill Pattern	Estimated Natural Frequencies (Hz)										
	Mode 1	Mode 2	Mode 3	Mode 4	Mode 5	Mode 6	Mode 7	Mode 8	Mode 9	Mode 10	Mode 11
Honeycomb	65.3 ± 0.1	75.5 ± 0.2	85.4 ± 0.3	155.6 ± 0.6	264.4 ± 0.7	402.5 ± 1.1	422.0 ± 0.7	451.7 ± 0.6	465.2 ± 0.9	545.2 ± 0.7	695.9 ± 1.0
Star	67.3 ± 0.1	76.5 ± 0.2	88.3 ± 0.2	161.9 ± 0.3	275.0 ± 0.4	418.0 ± 0.4	433.7 ± 1.0	462.8 ± 0.4	473.9 ± 0.6	559.5 ± 0.4	714.3 ± 0.6
Concentric	66.3 ± 0.2	†	83.6 ± 0.2	155.9 ± 0.4	267.0 ± 0.5	349.9 ± 1.0	407.6 ± 0.5	415.7 ± 1.0	432.2 ± 1.0	511.7 ± 0.9	674.6 ± 0.9

**Table 10.** Mean values of estimated damping ratios and standard deviations calculated from 10 modal tests of the analysed clamped specimens with different infill patterns. † = mode was not found.

Infill Pattern	Estimated Damping Ratios (%)										
	Mode 1	Mode 2	Mode 3	Mode 4	Mode 5	Mode 6	Mode 7	Mode 8	Mode 9	Mode 10	Mode 11
Honeycomb	1.484 ± 0.032	1.444 ± 0.020	1.258 ± 0.023	0.865 ± 0.036	0.710 ± 0.009	0.614 ± 0.022	0.755 ± 0.025	0.641 ± 0.020	0.703 ± 0.033	0.548 ± 0.021	0.583 ± 0.018
Star	1.453 ± 0.021	1.462 ± 0.018	1.287 ± 0.016	0.859 ± 0.014	0.698 ± 0.012	0.614 ± 0.016	0.865 ± 0.018	0.699 ± 0.011	0.841 ± 0.022	0.612 ± 0.012	0.559 ± 0.017
Concentric	1.536 ± 0.037	†	1.182 ± 0.015	0.793 ± 0.060	0.700 ± 0.024	1.111 ± 0.045	0.665 ± 0.019	0.879 ± 0.044	0.968 ± 0.038	0.579 ± 0.021	0.532 ± 0.024

### 4. Discussion

This article deals with the experimental estimation of the modal parameters of structures manufactured by the FDM method from two perspectives. In the first one, corresponding to the pre-test phase of the measurements, the authors aimed to analyse the influence

of the selected measurement settings on the modal parameters of a circular plate with a honeycomb infill pattern realized in the 0–800 Hz frequency span. Since the specimen was printed from PLA filament, in order not to influence it, the measurement of the responses of the structure was carried out in a non-contact way using a vibrometer working on the laser Doppler principle. The analysis was divided into four stages:

- The reference MISO analysis of the structure with 48 DOFs and one reference degree of freedom, realized with a frequency resolution of 2 Hz;
- The MISO analysis of the structure with 24 and 96 DOFs, respectively, and one reference degree of freedom, realized with a frequency resolution of 2 Hz;
- The MISO analysis of a structure with 48 DOFs and one reference degree of freedom realized with a frequency resolution of 1 Hz and 0.5 Hz, respectively;
- The MIMO analysis of a structure with 48 DOFs realized with a frequency resolution of 2 Hz, with emphasis on the choice of different numbers and locations of reference degrees of freedom.

It was found that reducing or increasing the number of excitation points (i.e., DOFs) resulted in vertical shifts between the CMIF plots and significant differences in the heights of the individual CMIF peaks as well. These phenomena could have occurred due to the accuracy of the singular value decomposition, which depends on a sufficient number of DOFs to capture the response of all modes in the system. It should be mentioned that only slight changes occurred concerning the natural frequencies (MVRD < 1%) and damping ratios (MVRD = 2–3%) estimated in the reference stage. However, the reduced number of DOFs caused the inaccuracy in the estimation of the mode shapes. On the other hand, the larger number of DOFs led to an increase in the mode shape accuracy and measurement time requirements as well.

A larger number of analysis lines, set through the use of FFT, contributes to increasing the frequency resolution. In this case, it was not possible to observe the mutual vertical shift of the singular lines; however, higher, sharper, and narrower CMIF peaks occurred. Moreover, the exponential weighting of the responses combined with the higher frequency resolution led to a minimization of the spectral leakage, contributing to larger sharpness of the peaks as well. Although there was no significant change in the natural frequencies obtained (MVRD < 0.4%), a radical decrease in the damping ratios, especially for the first five modes (MVRD = 16–20%), was observed.

By comparison of CMIF plots obtained from the MIMO analysis, it was found that each combination of reference degrees of freedom used contributes to the magnitudes of singular values differently. In two stages, six repeated modes of the structure were estimated. On the other hand, there were some stages in which not all of the modes were found. This finding confirmed that the choice of the appropriate number as well as the position of the reference degrees of freedom plays an important role in the estimation of the modal parameters. When comparing the modal parameters, it was found that the achieved relative differences in the natural frequency values (MVRD = 0.21–0.43%) and damping ratios (MVRD = 2.27–5.95%) were approximately at the same level as those for the other measurements. The advantage over the previous phases was the acquisition of the modal parameters of the repeated modes and the higher accuracy of the obtained mode shapes. The disadvantage was the increase in the time duration of the experiments, as it was doubled and tripled, respectively.

In the second (comparison) phase of the measurements, three structures (i.e., circular plates) with the same shape and dimensions manufactured by the FDM method were analysed. The structures with 15% honeycomb, star, and concentric infill pattern densities differed very slightly in mass (see Table 2). To compare the modal parameters of these structures, it was necessary to perform measurements under the same boundary conditions and with the same measurement parameters set. Although, due to the realization of the MIMO analysis in the pre-test phase, the obtained singular curves contained richer mode shape information, leading to a more accurate and detailed reconstruction of the mode shapes, based on the comparison of the obtained results and the time requirements of the



analyses, the authors decided to perform 10 MISO analyses of each structure. The results of the measurements represented by the repeating (almost identical) CMIF plots validated that there was no error on the part of the experimenters in the individual measurements.

A comparison of the mean singular curves of the CMIF plots obtained from the 10 measurements, carried out for each specimen, can be seen in Figure 20. From this comparison, as well as from Table 9, it is obvious that the natural frequencies of the analysed circulate plate with a concentric infill pattern are significantly lower than those of the other two structures. This confirms the fact that the specimens with honeycomb or star infill patterns have higher stiffness than those with concentric infill patterns. The relatively small values of the damping ratios obtained for each specimen indicate their prolonged vibrations and strong response to excitation at or near their natural frequencies. The standard deviations evaluated for each analysed modal parameter reach very small values, indicating the validity of the results presented here.

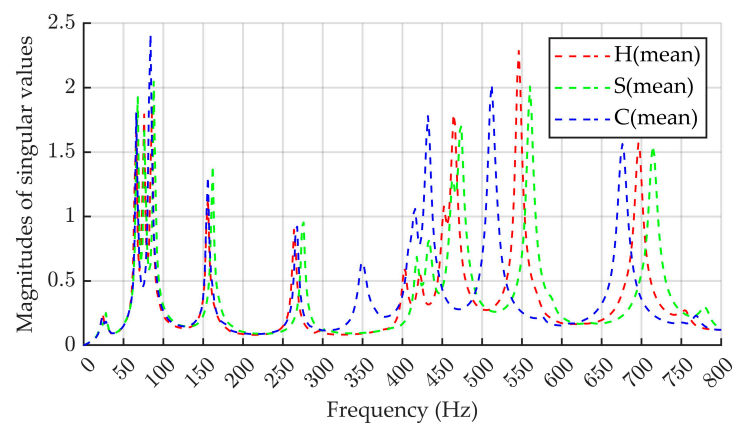


**Figure 20.** Mean CMIF plots of the analysed specimens with different infill patterns obtained from 10 measurements realized using the same measurement conditions.

Comparing the obtained mode shapes of the analysed structures, it can be concluded that these are the same for the structures with honeycomb (Figure 21) and star (Figure 22) infill patterns. The authors observed that the modes of these structures also presented relatively low complexity values, i.e., from 0.03 to 0.19. Changes can be seen in the case of the plate with a concentric infill pattern (Figure 23). Mode 2 was not found and mode 3 showed a different behaviour than expected. While, for the other modes of this structure, the complexity values ranged between 0.09 and 0.23, a complexity value of 0.48 was found for this mode. Thus, it can be assumed that the coupling of modes 2 and 3 occurred. In addition, mode 7 of this structure also showed a higher complexity value of 0.56, which could lead to mode crossing between modes 6 and 7, i.e., the swapping of their order in the frequency spectrum.

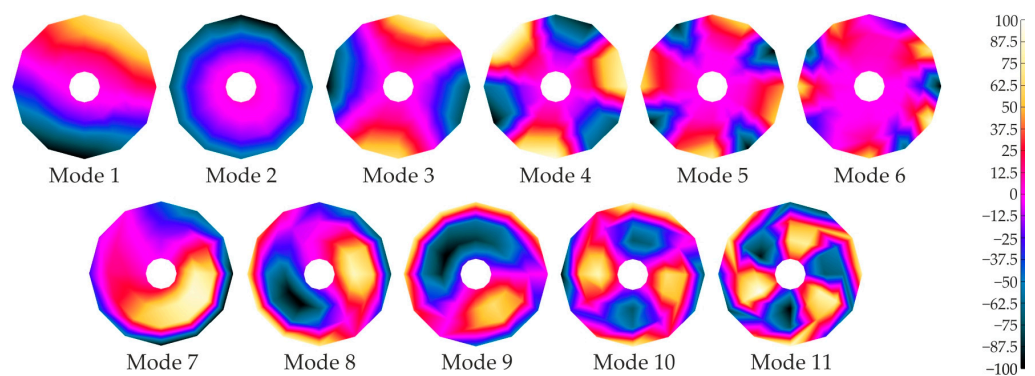


**Figure 21.** Mode shapes of the clamped specimen with honeycomb infill pattern.

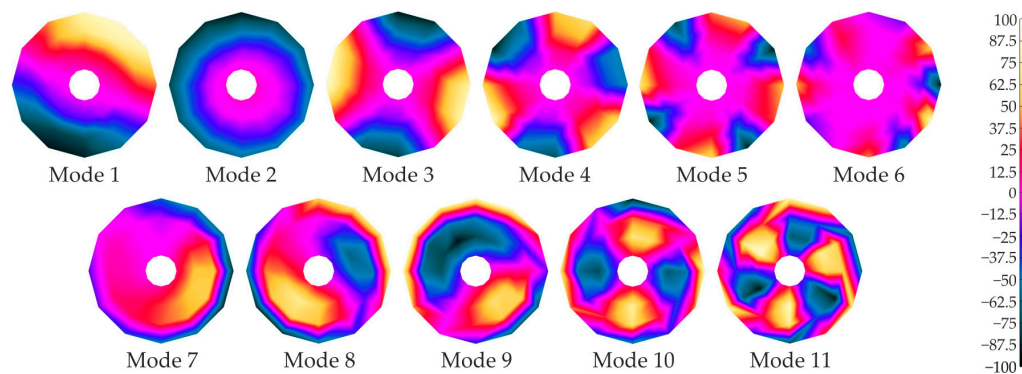


**Figure 22.** Mode shapes of the clamped specimen with star infill pattern.

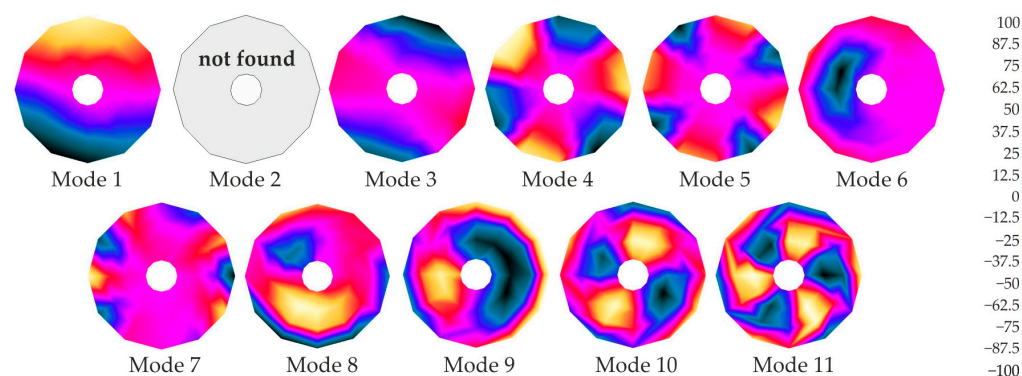


**Figure 23.** Mode shapes of the clamped specimen with concentric infill pattern.

Since repeated dismounting/clamping of the specimens to a robust structure (modal shaker) by applying the same torque did not cause significant differences in the obtained results, it can be assumed that the presented results can also be validated by other experimental means of modal analysis. In particular, this is a comparison of the results obtained from LDV when the analysed plates are excited by the modal shaker or when both excitation methods are used, with the response being acquired using the 3D digital image correlation method.

## 5. Conclusions

Nowadays, additive manufacturing methods are increasingly being applied not only in the early stages of product/structure design but also to manufacture the final product, which thus becomes relatively economically affordable and easy to produce. Product shapes are becoming more and more complicated and the results obtained from analyses of mechanical or modal properties carried out on simplified cantilever beams may no longer be sufficient to describe their dynamic behaviour. We consider it necessary to analyse other types of structures, which is quite time-consuming. Therefore, the development of methodologies that allow researchers to obtain correct results in the shortest possible time should be an essential part of experimenters' work. From the results obtained in this study, it can be said that it is possible to:

- Establish a suitable and time-accessible methodology for determining the modal parameters of specimens produced using differently selected 3D printing parameters such as the layer height, fill density, printing speed, bed and nozzle temperature, raster angle, infill pattern, etc.;
- To use the results obtained by specialized means in performing experimental modal analysis for comparison with the results obtained by non-conventional methods of determining modal parameters, such as the digital image correlation method, which

can not only speed up the time of conducting experiments but also, due to the number of measurement points, make the results of the analysis more accurate;

- Apply the conclusions obtained from the previous two points to define a suitable set of printing properties that will ensure the production of a product with the desired mechanical as well as modal properties;
- Use the measured data to fit/refine numerical models of the structures in question using parametric optimization tools. Using the FE model updating method, a homogenized model of the plates can also be created.

Based on the results presented in this article, it can be concluded that, in the implementation of the experimental modal analysis of PLA specimens manufactured by the FDM method, it is important to:

- Choose the number of excitation points (DOFs) appropriately. Note that, although the number of selected excitation points does not significantly affect the values of the modal parameters (natural frequencies, damping ratios), there are changes in the estimated mode shapes of vibration;
- Set the adequate number of lines in applying FFT. Note that an inappropriately set number of lines may lead to the underestimation of damping ratios;
- Define the location and number of response measurement points (reference degrees of freedom). An incorrectly chosen reference degree of freedom may lead to a reduction in the estimation of the modes of vibration. To obtain information about repeated modes, it is necessary to carry out a multiple-reference (MIMO) analysis. On the other hand, it should be taken into account that a larger number of reference degrees of freedom may lead to a significant increase in the time requirements;
- Monitor the value of mode complexity. A higher value of complexity may indicate coupling or crossing of the modes.

**Author Contributions:** Conceptualization, M.H. and M.P.; methodology, M.H. and R.H.; software, M.H., P.L. and P.P.; formal analysis, M.P. and P.P.; investigation, M.H.; resources, P.L.; writing—original draft preparation, M.H. and R.H.; writing—review and editing, M.H. and R.H.; visualization, P.P.; supervision, M.H. and R.H.; funding acquisition, M.P. and P.L. All authors have read and agreed to the published version of the manuscript.

**Funding:** This article has been produced with the financial support of the projects Slovak Research and Development Agency APVV-23-0461, Ministry of Education, Research, Development and Youth of the Slovak Republic VEGA 1/0152/24, VEGA 1/0516/22 and European Union under the REFRESH—Research Excellence for REgion Sustainability and High-tech Industries project number CZ.10.03.01/00/22\_003/0000048 via the Operational Programme Just Transition.

**Institutional Review Board Statement:** Not applicable.

**Informed Consent Statement:** Not applicable.

**Data Availability Statement:** The data that support the findings of this study are available from the corresponding author upon request.

**Conflicts of Interest:** The authors declare no conflicts of interest.

## References

1. New Boeing 777X Completes Successful First Flight. Available online: <https://investors.boeing.com/investors/news/press-release-details/2020/New-Boeing-777X-Completes-Successful-First-Flight/default.aspx> (accessed on 17 September 2024).
2. Pradeep, P.I.; Kumar, V.A.; Venkateswaran, T.; Aswin, S.; Nair, V.S.; Krishnan, A.; Akhil, Agilan, M.; Singh, S.K.; Narayanan, P.R. Processing and Characterization of 3D-Printed Inconel-718 Component through Laser Powder Bed Fusion Route for High-Temperature Space Application. *Trans. Indian Natl. Acad. Eng.* **2021**, *6*, 133–146. [CrossRef]
3. Apalboym, M.; Kujiraoka, S. Advances in the Development of Missile Telemetry Test Sets: Utilizing 3D Printing for Rapid Prototyping and Manufacturing. In Proceedings of the International Telemetering Conference, Las Vegas, NV, USA, 26–29 October 2015.
4. Ramesh Kumar, S.; Srinivas, V.; Jagan Reddy, G.; Raghavender Rao, M.; Raghu, T. 3D Printing of Fuel Injector in IN718 Alloy for Missile Applications. *Trans. Indian Natl. Acad. Eng.* **2021**, *6*, 1099–1109. [CrossRef]

5. NASA's Perseverance Rover Bringing 3D-Printed Metal Parts to Mars. Available online: <https://www.nasa.gov/centers-and-facilities/jpl/nasas-perseverance-rover-bringing-3d-printed-metal-parts-to-mars/> (accessed on 17 September 2024).
6. Broatch, A.; García-Tíscar, J.; Quintero, P.; Felgueroso, A. Rapid aerodynamic characterization of surface heat exchangers for turbofan aeroengines through optical techniques and additive manufacturing. *Therm. Sci. Eng. Prog.* **2024**, *55*, 102966. [[CrossRef](#)]
7. Tilton, M.; Lewis, G.S.; Wee, H.B.; Armstrong, A.; Hast, M.W.; Manogharan, G. Additive manufacturing of fracture fixation implants: Design, material characterization, biomechanical modeling and experimentation. *Addit. Manuf.* **2020**, *33*, 101137. [[CrossRef](#)]
8. Xu, J.; Tu, Z.; Zhang, S.; Tan, J.; Wang, G. Customized Design for Ergonomic Products via Additive Manufacturing Considering Joint Biomechanics. *Chin. J. Mech. Eng. Addit. Manuf. Front.* **2023**, *2*, 100085. [[CrossRef](#)]
9. Vij, M.; Dand, N.; Sharma, S.; Nair, N.; Sahu, S.; Wadhwa, P. Role of 3D printing in biomechanics. In *3D Printing in Podiatric Medicine*, 1st ed.; Sandhu, K., Singh, S., Prakash, C., Subburaj, K., Ramakrishna, S., Eds.; Academic Press: Cambridge, MA, USA, 2023; pp. 1–33.
10. Jiang, Y.; Islam, N.; He, R.; Huang, X.; Cao, P.F.; Advincula, R.C.; Dahotre, N.; Dong, P.; Wu, H.F.; Choi, W. Recent Advances in 3D Printed Sensors: Materials, Design, and Manufacturing. *Adv. Mater. Technol.* **2023**, *8*, 2200492. [[CrossRef](#)]
11. Jelva Hussan, K.S.; Subramaniam, M.P.; Mohammed Kenz, K.T.; Sreeram, P.; Parvathi, S.; Sari, P.S.; Pullanchiyodan, A.; Mulhivill, D.M.; Raghavan, P. Fabrication and challenges of 3D printed sensors for biomedical applications—Comprehensive review. *Results Eng.* **2024**, *21*, 101867. [[CrossRef](#)]
12. Bas, J.; Dutta, T.; Llamas Garro, I.; Velázquez-González, J.S.; Dubey, R.; Mishra, S.K. Embedded Sensors with 3D Printing Technology: Review. *Sensors* **2024**, *24*, 1955. [[CrossRef](#)]
13. Yang, J.; Li, B.; Liu, J.; Tu, Z.; Wu, X. Application of Additive Manufacturing in the Automobile Industry: A Mini Review. *Processes* **2024**, *12*, 1101. [[CrossRef](#)]
14. Sivasubramanian, P.; Kumar, P.; Pradeepkumar, C. Additive manufacturing in automotive and aerospace technologies: Advancements, applications, and case studies. In *Additive Manufacturing Materials and Technology*; Rangappa, S.M., Ayyappan, V., Siengchin, S., Eds.; Elsevier: Amsterdam, The Netherlands, 2024; pp. 85–98.
15. Alami, A.H.; Olabi, A.G.; Alashkar, A.; Alasad, S.; Aljaghoub, H.; Rezk, H.; Abdelkareem, M.A. Additive manufacturing in the aerospace and automotive industries: Recent trends and role in achieving sustainable development goals. *Ain Shams Eng. J.* **2023**, *14*, 102516. [[CrossRef](#)]
16. Zhao, N.; Parthasarathy, M.; Patil, S.; Coates, D.; Myers, K.; Zhu, H.; Li, W. Direct additive manufacturing of metal parts for automotive applications. *J. Manuf. Syst.* **2023**, *68*, 368–375. [[CrossRef](#)]
17. Virgala, I.; Kelemen, M.; Prada, E.; Sukop, M.; Kot, T.; Bobovský, Z.; Varga, M.; Ferenčík, P. A snake robot for locomotion in a pipe using trapezium-like travelling wave. *Mech. Mach. Theory* **2021**, *158*, 104221. [[CrossRef](#)]
18. Varga, M.; Sinčák, P.J.; Merva, T.; Marcinko, P.; Miková, L.; Prada, E.; Schnitzer, M.; Virgala, I. Design and analyses of tendon-driven continuum robots for minimally invasive surgery. In Proceedings of the 18th IFAC Conference on Programmable Devices and Embedded Systems (PDES), Brno, Czech Republic, 19–21 June 2024.
19. Hartomacıoğlu, S.; Kaya, E.; Eker, B.; Dağlı, S.; Sarıkaya, M. Characterization, generative design, and fabrication of a carbon fiber-reinforced industrial robot gripper via additive manufacturing. *J. Mater. Res. Technol.* **2024**, *33*, 3714–3727. [[CrossRef](#)]
20. Brezas, S.; Katsipis, M.; Kaleris, K.; Papadaki, H.; Katerelos, D.T.G.; Papadogiannis, N.A.; Bakarezos, M.; Dimitriou, V.; Kaselouris, E. Review of Manufacturing Processes and Vibro-Acoustic Assessments of Composite and Alternative Materials for Musical Instruments. *Appl. Sci.* **2024**, *14*, 2293. [[CrossRef](#)]
21. Tymrak, B.M.; Kreiger, M.; Pearce, J.M. Mechanical properties of components fabricated with open-source 3-D printers under realistic environmental conditions. *Mater. Des.* **2014**, *58*, 242–246. [[CrossRef](#)]
22. Lanzotti, A.; Grasso, M.; Staiano, G.; Martorelli, M. The impact of process parameters on mechanical properties of parts fabricated in PLA with an open-source 3-D printer. *Rapid Prototyp. J.* **2015**, *21*, 604–617. [[CrossRef](#)]
23. Daly, M.; Tarfaoui, M.; Chihi, M.; Bouraoui, C. FDM technology and the effect of printing parameters on the tensile strength of ABS parts. *Int. J. Adv. Manuf. Technol.* **2023**, *126*, 5307–5323. [[CrossRef](#)]
24. Chacón, J.M.; Caminero, M.A.; García-Plaza, E.; Núñez, P.J. Additive manufacturing of PLA structures using fused deposition modelling: Effect of process parameters on mechanical properties and their optimal selection. *Mater. Des.* **2017**, *124*, 143–157. [[CrossRef](#)]
25. Rodríguez-Panes, A.; Claver, J.; Camacho, A.M. The influence of manufacturing parameters on the mechanical behaviour of PLA and ABS pieces manufactured by FDM: A comparative analysis. *Materials* **2018**, *11*, 1333. [[CrossRef](#)]
26. Fernandez-Vicente, M.; Calle, W.; Ferrandiz, S.; Conejero, A. Effect of infill parameters on tensile mechanical behavior in desktop 3D printing. *3D Print. Addit. Manuf.* **2016**, *3*, 183–192. [[CrossRef](#)]
27. Peng, W.; Bin, Z.O.U.; Shouling, D.; Lei, L.I.; Huang, C. Effects of FDM-3D printing parameters on mechanical properties and microstructure of CF/PEEK and GF/PEEK. *Chinese J. Aeronaut.* **2021**, *34*, 236–246.
28. Behzadnasab, M.; Yousefi, A.A. Effects of 3D printer nozzle head temperature on the physical and mechanical properties of PLA based product. In Proceedings of the 12th International Seminar on Polymer Science and Technology, Tehran, Iran, 2–5 November 2016.
29. Yang, C.; Tian, X.; Li, D.; Cao, Y.; Zhao, F.; Shi, C. Influence of thermal processing conditions in 3D printing on the crystallinity and mechanical properties of PEEK material. *J. Mater. Process. Technol.* **2017**, *248*, 1–7. [[CrossRef](#)]



30. Hill, N.; Haghi, M. Deposition direction-dependent failure criteria for fused deposition modeling polycarbonate. *Rapid Prototyp. J.* **2014**, *20*, 221–227. [[CrossRef](#)]
31. Zhang, X.; Chen, L.; Mulholland, T.; Osswald, T. Effects of raster angle on the mechanical properties of PLA and Al/PLA composite part produced by fused deposition modeling. *Polym. Advan. Technol.* **2019**, *30*, 2122–2135. [[CrossRef](#)]
32. Birosz, M.T.; Ledenyák, D.; Andó, M. Effect of FDM infill patterns on mechanical properties. *Polym. Test.* **2022**, *113*, 107654. [[CrossRef](#)]
33. Foltut, D.; Valean, E.; Dzitac, V.; Marsavina, L. The influence of temperature on the mechanical properties of 3D printed and injection molded ABS. *Mater. Today Proc.* **2023**, *78*, 210–213. [[CrossRef](#)]
34. Bakar, A.A.B.A.; Bin Zainuddin, M.Z.; Bin Adam, A.N.; Noor, I.S.B.M.; Bin Tamchek, N.; Bin Alauddin, M.S.; Ghazali, M.I.B.M. The study of mechanical properties of poly(lactic) acid PLA-based 3D printed filament under temperature and environmental conditions. *Mater. Today Proc.* **2022**, *67*, 652–658. [[CrossRef](#)]
35. Ale Ali, R.; Karimi, H.R.; Mohamadi, R. PLA-based additively manufactured samples with different infill percentages under freeze-thaw cycles; mechanical, cracking, and microstructure characteristics. *Theor. Appl. Mech. Lett.* **2024**, *in press*. [[CrossRef](#)]
36. Ozcanli, O. *Modal Analysis of 3D Printed Parts. M07MAE—Individual Project*; Coventry University: Coventry, UK, 2017.
37. Iyibilgin, O.; Dal, H.; Gepek, E. Experimental modal analysis of 3D printed beams. In Proceedings of the 4th International Congress on 3D Printing (Additive Manufacturing) Technologies and Digital Industry 2019, Antalya, Turkey, 11–14 April 2019.
38. Rajkumar, S.M. Effect of Infill Pattern and Build Orientation on Mechanical Properties of FDM Printed Parts: An Experimental Modal Analysis Approach. *arXiv* **2022**, arXiv:2202.05692. Available online: <https://arxiv.org/pdf/2202.05692> (accessed on 19 September 2024).
39. Nguyen, H.T.; Crittenden, K.; Weiss, L.; Bardaweel, H. Experimental Modal Analysis and Characterization of Additively Manufactured Polymers. *Polymers* **2022**, *14*, 2071. [[CrossRef](#)]
40. Katunin, A.; Huňady, R.; Hagara, M. Damage Identification in Composite Structures Using High-Speed 3D Digital Image Correlation and Wavelet Analysis of Mode Shapes. *Nondestruct. Test. Eval.* **2024**, *in press*. [[CrossRef](#)]

**Disclaimer/Publisher’s Note:** The statements, opinions and data contained in all publications are solely those of the individual author(s) and contributor(s) and not of MDPI and/or the editor(s). MDPI and/or the editor(s) disclaim responsibility for any injury to people or property resulting from any ideas, methods, instructions or products referred to in the content.